Nuclear Instruments and Methods in Physics Research B 569 (2025) 165884

Contents lists available at ScienceDirect

Nuclear Inst. and Methods in Physics Research, B

journal homepage: www.elsevier.com/locate/nimb

Full length article

# Multiple-reflection time-of-flight mass spectrometer assisted laser spectroscopy of $^{nat}$Sm

Danny Münzberg [a,b,c,*], Alexandre Brizard [d], Tim van de Vendel [a,e], Jana Weyrich [a,b,c], Michael Block [a,b,c], Julia Even [e], Christian Helmel [f], Nathalie Lecesne [d], Sebastian Raeder [a,b], Daniel Rodríguez [g], Hervé Savajols [d], Klaus Wendt [c]

[a] GSI Helmholtzzentrum für Schwerionenforschung GmbH, Planckstraße 1, Darmstadt 64291, Germany
[b] Helmholtz Institut Mainz, Staudingerweg 18, Mainz 55128, Germany
[c] Johannes Gutenberg-Universität Mainz, Saarstraße 21, Mainz 55128, Germany
[d] GANIL, CEA/DRF-CNRS/IN2P3, Bd Henri Becquerel, Caen 14000, France
[e] University of Groningen, Broerstraat 5, Groningen 9712 CP, The Netherlands
[f] Technische Universität Darmstadt, Karolinenplatz 5, Darmstadt 64289, Germany
[g] Universidad de Granada, Granada 18071, Spain

ARTICLE INFO

*Keywords:*
RIS
Laser spectroscopy
JetRIS
MR-ToF MS

ABSTRACT

In this article we report laser Resonance Ionization Spectroscopy (RIS) experiments on $^{nat}$Sm with the assistance of a ToF-gated ion detection. This detection scheme enabled measurements of a given atomic transition for each isotope simultaneously without the need for isotopically enriched samples. Using this approach, multiple different excitation schemes were developed and specific mass and field shifts and the hyperfine parameter $\mathcal{A}$ of the transitions were determined. Furthermore this setup was used to commission a MR-ToF MS, which shall be integrated in the in-gas-Jet Resonance Ionization Spectroscopy (JetRIS) setup at GSI to enhance its capabilities for on-line measurements. This upgrade will enable on-line laser spectroscopy experiments on neutron-deficient samarium isotopes and heavy nuclides independent of their decay mode with a suitable half-life time, that are inaccessible with present techniques, such as $^{254}$Md.

## 1. Introduction

Laser spectroscopy is a tool for studying the structure of the electron shell of an atom and its nucleus. A particular interest arises in the region of the heaviest elements where the experimental knowledge of atomic and nuclear properties is scarce. The existence of these heavy nuclides is due to nuclear shell structure effects, stabilizing them against spontaneous fission [1–3]. Laser spectroscopy gives access to atomic levels, atomic state lifetimes and the ionization potential, for example. Such properties are affected by strong relativistic effects in the heaviest elements. Furthermore, electron correlations and quantum electrodynamics effects that are challenging theoretical calculations, play an important role. Also, laser spectroscopy enables determining nuclear properties such as spins and electromagnetic moments for probing the nuclear shell structure and the evolution of deformation. Isotopes of the heaviest elements can only be produced in minute quantities hampering experimental investigations. To enable detailed optical studies, the in-gas-**jet** **R**esonance **I**onization **S**pectroscopy (JetRIS) technique has been developed at GSI, Darmstadt, Germany [4]. Presently, JetRIS relies on radiation detection which enabled the measurement of an atomic transition of $^{254}$No with improved spectral resolution [5] utilizing the $\alpha$-decay detection of laser ions to achieve a low background measurement. In the future, such measurements are foreseen to be extended to additional heavy nuclei. For example the element mendelevium (Md, $Z = 101$), yet unstudied by laser spectroscopy, is of interest. It can be accessed producing the isotope $^{254}$Md via the electron capture decay of $^{254}$No. So far, no atomic levels of the element mendelevium have been reported and only theoretical predictions exist [6]. Laser spectroscopy can reveal these electronic levels [7]. This isotope, only decays via electron capture [8], complicating a decay-based detection. For this purpose, a **M**ultiple-**R**eflection **T**ime-**o**f-**F**light **M**ass **S**pectrometer (MR-ToF MS) [9] will be integrated in the JetRIS setup. This enables mass selected direct ion detection with high sensitivity making a low background measurement possible. Another advantage of the MR-ToF MS arises from additional beam purification during the measurement, utilizing in-trap deflector electrodes. Offline studies revealed that the heated filament in JetRIS despite the applied repulsive

* Corresponding author at: GSI Helmholtzzentrum für Schwerionenforschung GmbH, Planckstraße 1, Darmstadt 64291, Germany.
*E-mail address:* D.Muenzberg@gsi.de (D. Münzberg).

https://doi.org/10.1016/j.nimb.2025.165884
Received 7 July 2025; Received in revised form 27 August 2025; Accepted 29 September 2025
Available online 10 October 2025

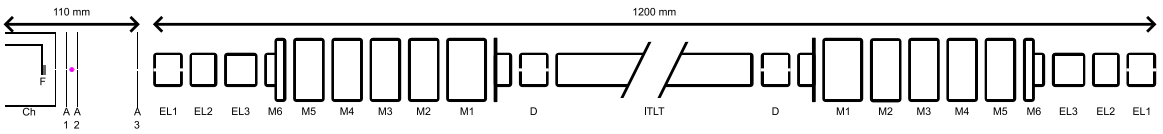


**Fig. 1.** Schematic of the MR-ToF MS with the laser ion source used in the experiment. The laser ion source consists of a filament (F), a filament channel (Ch) and three apertures (A1-3). The coloured circle shows the overlap region of the lasers. The MR-ToF MS is symmetrical with respect to its middle. Starting from the outside going inwards, there is an einzel lens (EL) consisting of three electrodes, followed by the stack of mirror electrodes (M) 1–6. Further inside there is a slitted deflector electrode (D) followed by an in-trap-lift-tube (ITLT).

potential can still yield ionic background affecting the identification of so far unknown species [10].

To investigate the potential of ToF-assisted laser spectroscopy and characterize the MR-ToF MS, two-step **R**esonant **I**onization **S**pectroscopy (RIS) on $^{nat}$Sm has been performed. Atomic transitions to excited atomic states in the range between $29\,695 - 30\,801\ \mathrm{cm}^{-1}$ were investigated utilizing mass-selected ion detection, which will be discussed in Sec. 2.4. Isotope shifts for stable Sm isotopes were obtained and the hyperfine structure of the odd-mass stable isotopes was determined. Since no samarium isotope with a mass number below $A = 138$ has been measured via laser spectroscopy so far [11], the development of laser excitation schemes is a prerequisite for future online studies. The most neutron-deficient samarium isotope experimentally known is $^{129}$Sm, even though the isotope with $A = 130$ has not been observed yet [8].

The samarium isotopes from $A = 129$ to $A = 137$ can be produced via fusion-evaporation reactions and feature lifetimes which are suitable for laser spectroscopy with JetRIS. Samarium isotopes of interest could be produced by a reaction of a sulphur beam on palladium [12]. For example, $^{132}$Sm could be produced, using naturally occurring isotopes $^{32}$S + $^{102}$Pd in the 2 n evaporation channel. Samarium-isotopes until the drip line are expected to be accessible through the reaction of $^{40}$Ca + $^{92}$Mo, which offers the potential to produce all remaining samarium isotopes below $A = 138$ when utilizing the many naturally occurring stable calcium and molybdenum isotopes.

To expand measurements with JetRIS to be independent on the decay, the setup will be extended, with a cooler buncher, followed by a pulsed drift tube and the MR-ToF MS, with an ion detector at the end, as discussed in Section 3. The design of the cooler buncher has been finalized and the expected performance will be discussed in Section 3.1. As JetRIS was used during online beamtime at GSI, Darmstadt with the decay assisted detection, the MR-ToF MS was commissioned independently within this work. The measured performance of the MR-ToF MS was compared to ion trajectory simulations using SIMION 8.1 [13,14], for validation of their predictive power. These results will be discussed in Section 3.2 together with the expected performance of the MR-ToF MS in combination with the cooler buncher and the pulsed drift tube.

## 2. Experimental setup

In this work the MR-ToF MS has been tested in stand-alone mode with a dedicated laser ion source utilizing the filament technique of JetRIS. The schematic overview of this setup is shown in Fig. 1. It consists of the laser ion source, the MR-ToF MS and the detector setup with two metal grids in front where the one closer to the detector can be set on an electric potential to measure the longitudinal energy distribution of the ions. To detect the ions, a commercial ion detector (MagneToF mini, ETP ion detect) is used. The readout of the detector signal to acquire ToF spectra was done using a time-to-digital converter (MCS8 A, FASTComTech). The MagneToF mini produces an analog signal with a negative voltage and the threshold for the discriminator of the MCS8 A was set to −7 mV. For the timing pattern, a 9520 Pulse Delay Generator (Quantum Composers) was used. The pressure in the system was typically $p = 5 \cdot 10^{-8}$ mbar, leading to a mean free path of roughly 1.2 km.

### 2.1. MR-ToF MS

The MR-ToF MS used within this study was designed at the Technical University of Darmstadt in the frame of the 'DA's MR-ToF collaboration'. The design of the MR-ToF MS is described in detail in Ref. [9]. In the following, a brief overview of the setup will be given. The MR-ToF MS, as shown in Fig. 1, is axially symmetric with respect to its middle point and consists of four main parts. On both ends an einzel lens (EL) is placed, where the outer most electrode consists of four equal pieces to allow for steering of the ion beam. Next to the einzel lens is the mirror-electrode stack, consisting of 6 cylindrical electrodes (M1–M6) which can be biased individually. Going further inwards is the in-trap-deflector electrode, another cylindrical electrode cut into four equal pieces to be able to deflect ions while trapped for beam purification. In the middle of the setup is the in-trap-lift tube (ITLT) which allows adjusting the kinetic energy of the ions to trap and eject them without pulsing the mirror electrodes [15]. The voltages applied to the MR-ToF MS electrodes are given in Table 1. For measurements in which the ions were trapped, the in-trap lift tube was pulsed from the value in Table 1 down to 0 V for the trapping procedure and from this back to the original value for the ejection.

### 2.2. Laser ion source

A schematic drawing of the laser ion source setup is shown in Fig. 1. It consists of a 25 µm thick tantalum strip, called the filament (F), which can be resistively heated and biased to an electric potential. The strip was folded in a way that a quadratic piece of samarium foil could be inserted, which is passively heated by the tantalum strip due to the physical contact. The filament is placed inside a cylindrical channel (Ch) with a central hole of 3 mm diameter in the endcap. This is followed by three parallel circular metal plates with a central hole of 1 mm diameter for the first two plates and 3 mm diameter for the last one. These plates are used to define the electric field gradient and to cut parts of the beam to reduce angular spread, therefore calling them acceleration aperture (A) 1, 2, and 3 in order of their proximity to the filament. When the filament is heated, the samarium foil releases neutral samarium atoms, as well as $Sm^+$ and electrons due to surface ionization. The channel including its endcap and the last acceleration aperture are grounded, the filament and the first two acceleration apertures are biased. The applied potentials can be found in Table 1. In this configuration, the emitted electrons are deflected between channel and filament and the surface ionized samarium is deflected between the channel endcap and the first acceleration aperture, leaving only the samarium atoms after the first acceleration aperture. In the centre between the first and second acceleration aperture, two laser beams are overlapped for two-step RIS. Due to the setup only having windows on one axis, the lasers could not be overlapped in a cross-beam geometry but had to be overlapped collinearly in a shallow angle of 1.4° between both beam paths. This results in a cylindrical ionization volume perpendicular to the extraction direction, with a diameter of about 2 mm and a length of several centimetres, where samarium is ionized. The laser system is described in detail in Section 2.3.

**Table 1**
Voltages applied to the setup electrodes. The names in the electrode row refer to the names shown in Fig. 1.

| electrode | Ch | F | A1 | A2 | A3 | EL1 | EL2 | EL3 | M1 | M2 | M3 | M4 | M5 | M6 | D | ITLT |
|---|---|---|---|---|---|---|---|---|---|---|---|---|---|---|---|---|
| $U$/V | 0 | 25 | 3090 | 3000 | 0 | 0 | 3000 | 0 | −4430 | 916 | 714 | 2090 | 2575 | 3066 | 0 | 1110 |

### 2.3. Laser system

For two-step RIS, two tunable lasers are required. For the first excitation step, which is used for spectroscopy, a narrowband laser is required, while a broadband laser was used for the second, ionizing transition. The narrowband laser system is comprised of a pulsed dye amplifier (PDA, Sirah Lasertechnik) pumped by a high-power single-mode, pulsed, frequency-doubled Nd:YAG laser (PXn300-2-GF-SLM, Edgewave). The PDA was seeded using a tunable, single-mode continuous-wave (cw) dye laser (Matisse, Sirah Lasertechnik) pumped by a cw, frequency-doubled Nd:YAG laser (Millenia, Spectra Physics). The light of the PDA was frequency-doubled using a single-pass second-harmonic generation (SHG) unit utilizing a $\beta$-barium borate (BBO) crystal. To obtain the laser light around 330 nm for the first excitation step of samarium, the lasers were operated with 4-Dicyanomethylene-2-methyl-6-p-dimethylaminostyryl-4H-pyran (DCM) in dimethyl sulfoxide (DMSO) for the PDA and DCM in a 1:1 mixture of phenoxyethanol (EPH) and ethylene glycol (EG) for the cw laser. The single-mode operation of the pump laser was required to avoid unwanted excitation caused by side modes [16]. The narrowband system achieved a spectral linewidth of $\delta f_{\mathrm{nb}} = 139(13)$ MHz after SHG, measured using a Fabry–Pérot interferometer (FSR 1 GHz, Toptica) and a pulse width of 5 ns at full-width half-maximum. The broadband laser system is comprised of a pulsed dye laser (Credo, Sirah Lasertechnik) pumped by a frequency-doubled Nd:YAG laser (InnoSlab IS400-2-L, Edgewave). The dye used for the Credo was DCM in Ethanol to produce laser light around 640 nm for the resonant ionization of samarium. The broadband laser system is specified with a linewidth of $\delta f_{\mathrm{bb}} = 1.8$ GHz according to the manual of the company. The pulse width was measured to be 8 ns at full-width half-maximum. A typical spot size for both lasers has a diameter of roughly 2 mm and a pulse energy of 8 µJ for the PDA after SHG and 1 mJ for the CREDO. The combination of laser ionization with a MR-ToF MS based detection without the use of a cooler buncher requires the laser to be synchronized with the MR-ToF MS cycle. The pump lasers can provide repetition rates from 10 kHz down to single shots. They were triggered and synchronized from the same delay generator that controls the MR-ToF and according to the number of revolutions in the MR-ToF MS, the repetition rate of both pulsed pump lasers could be freely adjusted. The wavelength of the lasers during the experiment was measured using a commercial wavemeter (WS7-30, HighFinesse) which was regularly calibrated using a frequency-stabilized helium-neon (HeNe, SIOS) laser.

### 2.4. RIS on $^{nat}$Sm

Laser spectroscopy on $^{\mathrm{nat}}$Sm was performed to demonstrate the operation of ToF-assisted laser spectroscopy and to develop and characterize ionization schemes for application on exotic, short-lived isotopes. In total, six different first-step transitions $\tilde{\nu}_1$ were investigated as summarized in Fig. 2. All of these transitions start from thermally excited levels within the ground state fine structure. Due to the angular momentum being $J = 0$ for the ground state, these excited levels feature a higher population at the evaporation temperature of 1000 °C used during the experiment. The mass spectrum from laser ionized $^{\mathrm{nat}}$Sm is shown in Fig. 3, where the ion count rate as a function of the ToF relative to the laser trigger pulse is plotted. Here, seven different peaks can be clearly distinguished, each of which can be assigned unambiguously to a different isotope of samarium. The ToF spectrum is given in terms of the registered count rate as counts per second (cps) versus the time of flight. The multiscaler has 4096 individual channels with a time resolution of 800 ps. The mass numbers of the natural isotopes of samarium are $A = 144, 147, 148, 149, 150, 152$ and 154, all of which were studied in this work. All ions are extracted with the same electric potentials of a maximum of $U = 3090$ V. With the velocity being described by $v = \sqrt{\frac{2 \cdot q \cdot U}{m}}$, the lightest isotope,$^{144}$Sm has the shortest flight time to the detector, and the peaks were assigned to the individual isotopes in ascending order of their mass number. This assignment is supported from the arrival times following the square root of the mass-to-charge ratio. The ToF spectrum does not, however, reflect the relative natural abundance of the isotopes, which is due to the fact that the odd $A$ isotopes have a nuclear spin of $I = 7/2$ giving rise to hyperfine structure and due to fluctuation of the ion source. For laser spectroscopy, the counts in a time-of-flight interval corresponding to an individual Sm isotope, indicated by shaded areas in Fig. 3, were summed for a given wavenumber of the first excitation step. Preparing for laser spectroscopy, suitable autoionizing (AI) resonances were identified for each first excitation step to ensure efficient laser ionization. The width of the AI states was experimentally measured to range from 30 to 90 GHz. Plotting the summed counts against the laser excitation energy for a transition results in the spectra for different isotopes as shown in Fig. 4 exemplary for the transition of scheme 3 of Fig. 2. The achieved spectral resolution amounts to a FWHM of 175(5) MHz. The spectra were fitted by least-square minimization with the SATLAS package [17] in Python. The peaks were modelled as Voigt profiles. The Gaussian and Lorentzian contributions were treated as free parameters without constraints. With this approach, the Lorentzian contribution was found to be negligible, so that the FWHM is dominated by the Gaussian contribution. The main factor for the Gaussian contribution is the laser bandwidth with 139(13) MHz. The other contribution is due to Doppler broadening, arising from the thermal energy of the samarium with the spot size for the ionization. The Doppler broadening was determined to be 36(14) MHz. The nuclear spin $I$ [18], the total angular momentum quantum number $J$ [19–21] of ground and excited atomic states and the hyperfine parameters of the ground states $\mathcal{A}_{\mathrm{l}}$ and $\mathcal{B}_{\mathrm{l}}$, summarized in Table 2, were taken as fixed parameters from literature [22]. The odd mass isotopes have a nuclear spin of $I = 7/2$ and the even mass ones have $I = 0$. From this fitted hyperfine structure, the centroid of the transition and the hyperfine parameter of the upper state $\mathcal{A}_{\mathrm{u}}$ were determined as shown in Table 3. For both isotopes with $I \neq 0$, $^{147}$Sm and $^{149}$Sm, the ratios of the hyperfine parameters were determined as a consistency check. They are consistent with the ratio obtained from the literature values of the ground states. Slight deviations up to 0.6% can be attributed to hyperfine anomaly. Since not all hyperfine lines were resolved and the isotopes feature small nuclear deformations [23,24], the hyperfine parameter $\mathcal{B}_{\mathrm{u}}$ is expected to be small and could not be determined with the achieved resolution, but is in agreement with being neglectable. For the determination of the uncertainty of the hyperfine parameter $\mathcal{A}$, the response to a value comparable to the ground state contribution was also evaluated. Two excited levels at 30 823.44(2) cm$^{-1}$ and at 31 185.11(1) cm$^{-1}$ were investigated each with two different transitions and the results for their hyperfine parameters show an excellent agreement (c.f. Table 3).

From the centroids of the individual resonances of an isotope with atomic mass number $A$, the isotope shift was determined relative to the resonance of $^{154}$Sm in the same transition by

$$\delta\nu^{154,\mathrm{A}} = \nu^{\mathrm{A}} - \nu^{154}. \tag{1}$$

Here again, a similar isotope shift for transitions to the same excited level is observed. This behaviour is expected, as the ground state fine

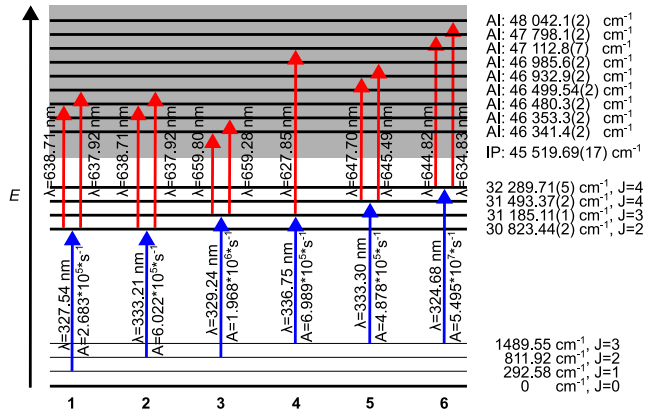


**Fig. 2.** Level scheme of the measured transitions in samarium. The value of the ionization potential (IP) was taken from [25]. The values of the thermally excited ground states were taken from [26] and the J-values of the levels from [19–21]. They correspond to the electronic configuration of $4f^6 6s^2$. The values of the excited states were determined for $^{154}$Sm from adding the wavenumber of the first excitation step (FES) transition $\tilde{\nu}_1^{154}$ and the wavenumber of the second excitation step (SES) transition $\tilde{\nu}_2^{154}$ to the literature value of the ground state. The individual values were converted to a wavelength and are given as the wavelength $\lambda$ of the transition.

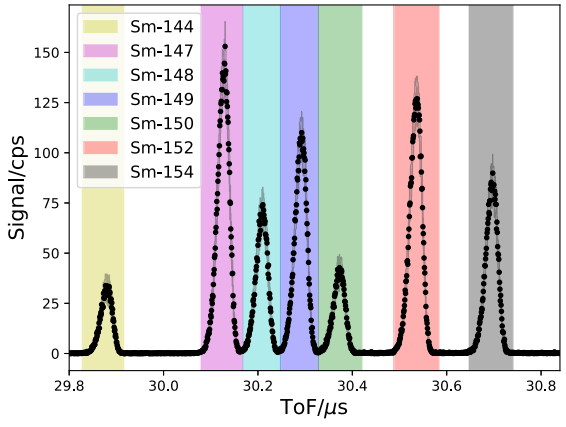


**Fig. 3.** Sum of all ToF spectra of the samarium isotopes from the measurements of the transition shown in Fig. 4. The shaded areas were used as gates for the respective isotope in the analysis of the laser spectroscopy. The individual peaks show a ToF width (FWHM) of 40 ns.

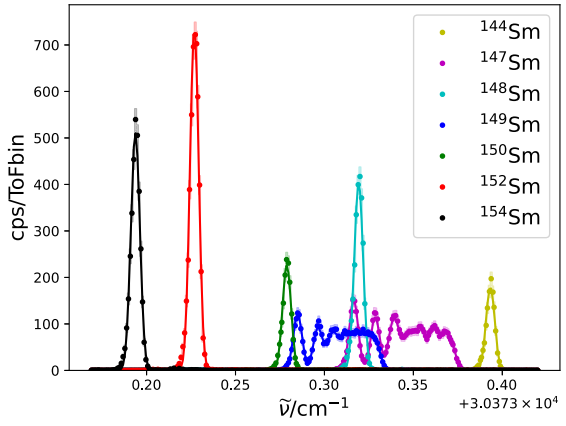


**Fig. 4.** Optical spectrum of the FES transition of scheme 3 in Fig. 2 for all naturally occurring samarium isotopes. The points show the measured data, while the lines are fits to the data using voigt peak shapes.

**Table 2**
$J$-values for the thermally excited ground state levels [19–21], as well as Hyperfine parameters of thermally excited atomic states used in the fit of the spectral data taken from literature [22]. The nuclear spin was taken as $I = 7/2$ for $^{147,149}$Sm and as $I = 0$ for the other natural isotopes [18]. The weighted averages of the ratios are $\mathcal{A}_{1,147}/\mathcal{A}_{1,149} = 1.21305(2)$ and $\mathcal{B}_{1,147}/\mathcal{B}_{1,149} = -3.4601(6)$.

| $E$/cm$^{-1}$ | $\mathcal{A}_{1,147}$/MHz | $\mathcal{A}_{1,149}$/MHz | $\mathcal{B}_{1,147}$/MHz | $\mathcal{B}_{1,149}$/MHz | $J$ |
|---|---|---|---|---|---|
| 292.58 | −33.493(2) | −27.610(1) | −58.688(6) | 16.963(3) | 1 |
| 811.92 | −41.186(2) | −33.952(2) | −62.229(13) | 17.990(13) | 2 |
| 1489.55 | −50.243(2) | −41.418(2) | −33.668(40) | 9.746(40) | 3 |

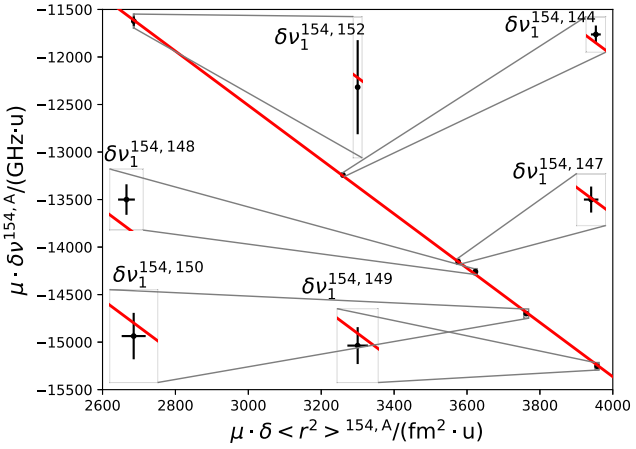


**Fig. 5.** Kingplot of the samarium isotopes relative to $^{154}$Sm for the FES transition of scheme 3 with $\tilde{\nu} = 30\,373.194(1)\,\mathrm{cm}^{-1}$. Uncertainties on the charge radii only take the relative uncertainty given in Ref. [27], while the systematic uncertainty on the absolute charge radii is not included.

structure multiplet is built from the same electron orbitals resulting in a very similar change in electron density within the nucleus when exciting to the same upper level. With these isotope shifts and the relative mean-square charge radii $\delta < r^2 >^{A,A'}$ [27], taken from literature, a Kingplot analysis [28] was performed according to

$$\mu \cdot \delta\nu^{A,A'} = K + F_s \cdot \mu \cdot \delta < r^2 >^{A,A'}, \tag{2}$$

where $\mu$ is the reduced mass given by

$$\mu = \frac{M_A M_{A'}}{M_A - M_{A'}}. \tag{3}$$

With these relations, the mass shift $K$ and the field shift $F_s$ were determined for the respective transition. The results are summarized in Table 3. One exemplary Kingplot can be seen in Fig. 5. To determine changes in nuclear mean-square charge radii, excitation schemes 1 and 2 will be the most suitable since they provide the largest isotope shift, making them the most sensitive to changes in nuclear size. These schemes, leading to the same first excited level, feature also the largest HFS splitting and sensitivity to nuclear magnetic dipole moments. The spectral resolution was insufficient to be sensitive to small contributions related to a non-zero spectroscopic quadrupole moment $Q_s$. For simultaneous production of a wide range of isotopes, excitation scheme 5 can be used since it has the smallest isotope shift.

## 3. The JetRIS system and future extensions

The schematic layout of the JetRIS setup with the future integration of the MR-ToF MS is shown in Fig. 6. The nuclides of interest are produced in fusion-evaporation reactions and separated from the high intensity primary beam using the **S**eperator for **H**eavy **I**on reaction **P**roducts (SHIP) [29,30]. Recoil ions with different charge states enter the gas cell through a thin entrance window where they are stopped

**Table 3**
Results of the spectroscopy of $^{nat}$Sm. The FES of schemes 1 and 2, as well as 3 and 4 result in the same atomic level, which gives them the same SES.

| Scheme | $\tilde{\nu}_1^{154}$/cm$^{-1}$ | $\delta\nu_1^{154,152}$/MHz | $\delta\nu_1^{154,150}$/MHz | $\delta\nu_1^{154,149}$/MHz | $\delta\nu_1^{154,148}$/MHz | $\delta\nu_1^{154,147}$/MHz | $\delta\nu_1^{154,144}$/MHz | $\mathcal{A}_{u,149}$/MHz | $\mathcal{A}_{u,147}$/MHz | $\mathcal{A}_{u,147}/\mathcal{A}_{u,149}$ | $K$/(GHz·u) | $F_s$/(GHz/fm$^2$) | $\tilde{\nu}_2$/cm$^{-1}$ |
|---|---|---|---|---|---|---|---|---|---|---|---|---|---|
| 1 | 30 530.852(1) | 1268(42) | 3454(42) | 4533(42) | 5043(42) | 5858(42) | 7852(42) | −158.1(5) | −193.4(4) | 1.223(3) | −2125(247) | −4.70(7) | 15 676.10(1) |
| | | | | | | | | | | | | | 15 656.84(8) |
| 2 | 30 011.536(1) | 1262(42) | 3445(42) | 4536(42) | 5052(42) | 5870(42) | 7861(42) | −158.4(8) | −192.7(5) | 1.217(4) | −1945(108) | −4.75(3) | |
| 3 | 30 373.194(1) | 995(42) | 2551(42) | 3331(42) | 3762(42) | 4386(42) | 5984(42) | −78.7(2) | −96.1(2) | 1.221(3) | −3946(65) | −2.85(2) | 15 156.25(8) |
| | | | | | | | | | | | | | 15 168.22(6) |
| 4 | 29 695.557(1) | 995(42) | 2569(42) | 3367(42) | 3798(42) | 4446(42) | 6017(42) | −79.7(16) | −96.0(13) | 1.20(2) | −3608(144) | −2.98(4) | 15 927.7(7) |
| 5 | 30 003.823(1) | 651(42) | 1559(42) | 2003(42) | 2302(42) | 2689(42) | 3750(42) | −107.4(2) | −130.1(2) | 1.211(2) | −4234(111) | −1.25(3) | 15 492.26(3) |
| | | | | | | | | | | | | | 15 439.56(9) |
| 6 | 30 800.159(1) | 1100(42) | 2908(42) | 3810(42) | 4293(42) | 5001(42) | 6793(42) | −114.9(4) | −140.3(3) | 1.221(4) | −3193(168) | −3.61(5) | 15 752.4(2) |
| | | | | | | | | | | | | | 15 508.41(1) |

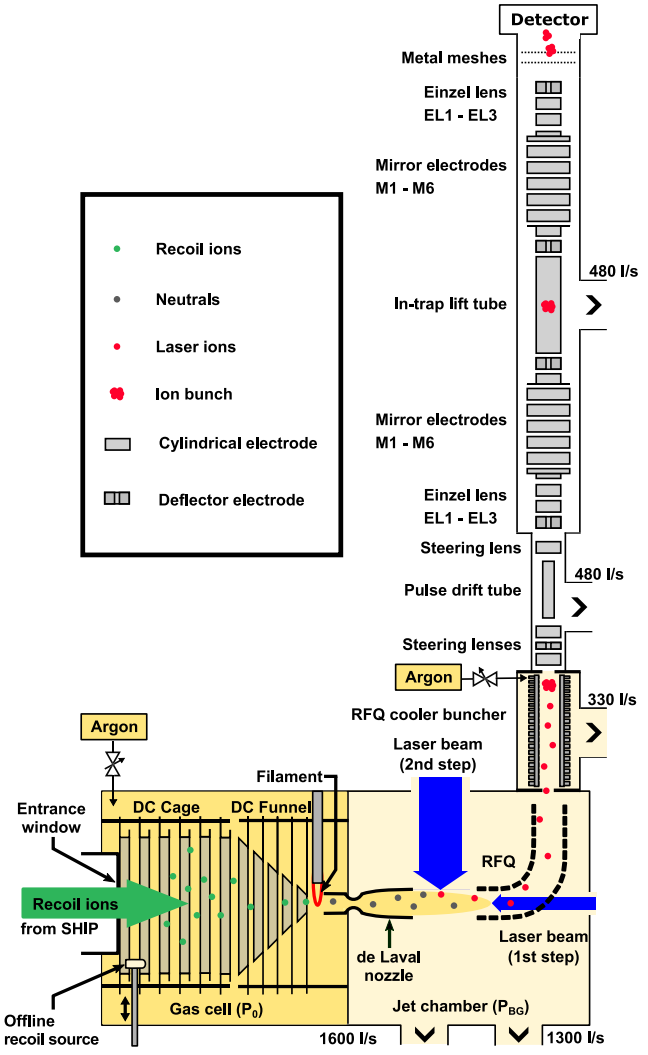


**Fig. 6.** Schematic overview of the envisioned full setup of JetRIS with the addition of the cooler buncher, pulsed drift tube and MR-ToF MS. The length of the setup along the JetRIS is 0.7 m, the side to the MR-ToF is 2.2 m.

and thermalized in argon buffer gas at 80 mbar of pressure. Most of the recoil ions remain in a singly charged state. Multiple electrodes surrounding this stopping volume guide the ions via an electric field towards a 125 µm thin tantalum wire, referred to as a filament, which is resistively heated to approximately 1200 °C, depending on the element under investigation [31]. The contact with the filament neutralizes and adsorbs the ions and the heat ensures desorption from the filament. After evaporation, the atoms are transported by gas flow through a de-Laval type nozzle towards the low pressure jet cell. This nozzle forms a low-pressure, low-temperature, hypersonic gas jet. The jet shape and the appropriate background pressures in the jet cell have been investigated in detail [32,33]. Within the gas jet region two laser beams are overlapped in cross-beam geometry, where the FES)' is anticollinear to the gas jet and the SES is in perpendicular configuration, performing two-step RIS. The conditions inside the gas jet feature a negligible pressure broadening and a low Doppler broadening enabling spectral linewidths of 211(35) MHz [33] under optimal conditions. Nevertheless, the velocity of the ions from the gas expansion is about 550 m/s [34]. With the interaction region being 60 mm long, a laser repetition rate of 10 kHz is required for efficient laser interaction. The produced laser ions are transported via a 90° bend radio frequency quadrupole (RFQ) structure into the next vacuum chamber. Presently, a silicon detector is used in high vacuum conditions for alpha-decay detection [5]. This configuration is suitable for $\alpha$-decaying nuclides with half-lives of more than 0.2 s. Measurements of long half-lives in the range of hours are possible but time consuming.

### 3.1. Design characteristics of the JetRIS cooler buncher

For the integration of the MR-ToF MS into JetRIS, as seen in Fig. 6, a radio frequency cooler buncher is required to collect and bunch the laser ions. In addition, the buncher ensures well-defined initial conditions for longitudinal and transversal emittance of the ion beam, which is mandatory for a high mass resolving power, while maintaining high efficiency. The layout of the cooler buncher was inspired by the design used at GANIL for the S$^3$-LEB setup [35], along with a pulsed drift section to accelerate the ion bunches to the kinetic energy of 3 keV needed to enter the MR-ToF MS, and is schematically shown in Fig. 6. The cooler buncher consists of a linear, 345 mm long RFQ, in which 4 times 20 plate electrodes are inserted in between the RFQ rods in order to create a DC-potential well to trap the ions, forming 20 segments along the RFQ. The first 12 segments with a linear potential gradient of the cooling section are 19 mm long, while the remaining eight segments, forming the actual potential well are 9 mm long to achieve a well-defined location of the ion bunch at the second last electrode. The last four electrodes from the buncher can be switched in potential to eject the ions towards the MR-ToF MS. The following pulsed drift section will be in high vacuum by means of an orifice acting as pumping barrier. It is composed of an einzel lens, the drift tube and an electrode at ground potential at its exit. The middle electrode of the einzel lens is azimuthally 4-fold segmented, serving as a deflector, allowing for correction of the ion trajectories. As JetRIS is operated with argon buffer gas, the cooler buncher was investigated for operation with argon as well. Ion trajectory simulations with SIMION 8.1 have been conducted to estimate the performance and properties of the cooler buncher. The electrodes were modelled with a 0.2 mm grid size. The interaction with the argon buffer gas atoms in the bunching section were modelled as elastic hard sphere collisions using the collision_hs1 library of SIMION. To determine an optimal argon gas pressure, simulations were conducted from $5.0 \cdot 10^{-4}$ mbar to $4.0 \cdot 10^{-3}$ mbar, for 10 and 100 ms storage time. Both storage times show similar behaviour for the pressure dependence, while the longer storage time is slightly better in efficiency as shown in Fig. 7. The best transmission efficiency of $\epsilon = 0.79(5)$ was found at a pressure of $p = 1.0 \cdot 10^{-3}$ mbar for 100 ms storage time. Further analysis also

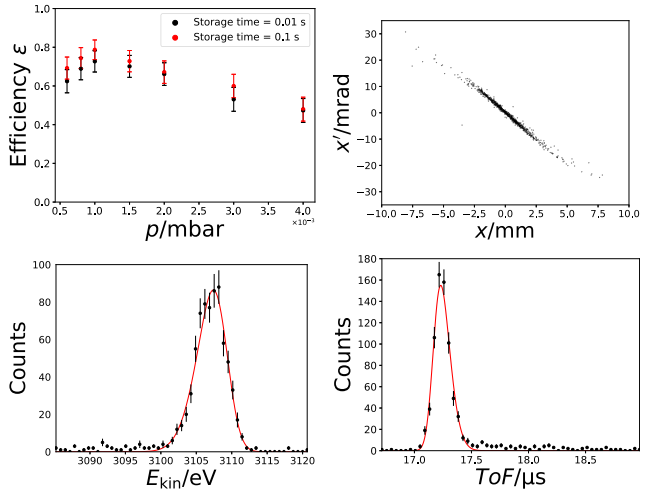


**Fig. 7.** Upper left: Simulated Transmission efficiency $\epsilon$ of the cooler buncher in bunching mode and the pulsed drift tube as a function of the residual gas pressure in the cooler buncher for two storage times of 10 ms (black) and 100 ms (red). Upper right: Simulated transversal emittance of the ions from the cooler buncher, after the pulsed drift tube. The emittance is the same in both axis due to the symmetry of the setup. Lower figures: Simulated distributions of kinetic energy (left) and ToF (right) after the pulsed drift tube for a pressure of $p = 1.0 \cdot 10^{-3}$ mbar and 100 ms storage time. The data points were fitted using skewed gaussian distributions (red line) [36].

highlights this value as optimal in terms of kinetic-energy and time-of-flight distributions which are shown in the lower panels of Fig. 7. Here, an energy spread of $\Delta E_{\mathrm{kin}} = 5.0(4)$ eV and a ToF width of $\Delta t = 172(14)$ ns were determined.

### 3.2. Ion-source characterization

Since the performance of the MR-ToF MS depends on the quality of the injected ion beam, it is also necessary to characterize the ion beam produced by the source and its ion-optical components. The mean longitudinal kinetic energy $E_{\mathrm{kin}}$, the energy spread $\Delta E_{\mathrm{kin}}$ and the ToF width were determined and optimized experimentally, while the transversal emittance was estimated from simulations using SIMION 8.1. During the optimization of the ion-source parameters, ions were only transmitted through the MR-ToF MS and not trapped. For the kinetic energy measurement, the potential applied to the metallic mesh in front of the detector was varied close to the kinetic energy of the ions acting as an energy filter. The mean energy of the ions was determined as $E_{\mathrm{kin}} = 3063.4(2)$ eV which is in agreement with the ionization region being located between A1(3000 V) and A2(3090 V). Assuming a Gaussian distribution of the kinetic energies an energy spread of $\Delta E_{\mathrm{kin}} = 25(1)$ eV was determined. In the simulations, the distribution was assumed to be evenly distributed inside the starting volume of the ions. Measured ToF spectra are shown in the top left panels of Fig. 8 (black data points), for an increasing number of revolutions. The left peak in the upper panel was fitted using a Gaussian giving a ToF distribution of 121(1) ns. The second peak can be attributed to ions generated from the same isotope, but with a slower extraction from the ionization volume due to their position on the outer edge of the volume. Simulations are also shown from which it becomes apparent that the existence of multiple ToF peaks is inherent to the design of this source. This is attributed to the large, cylindrical, ionization volume, in which ions further away from the central axis are transported slower towards the accelerating potential. The simulations were done with a 0.1 mm grid size and are based on a cylindrical starting volume of the ions with a diameter of 2 mm and a length of 5 mm orthogonal to the central axis of the setup. This resembles the conditions of the

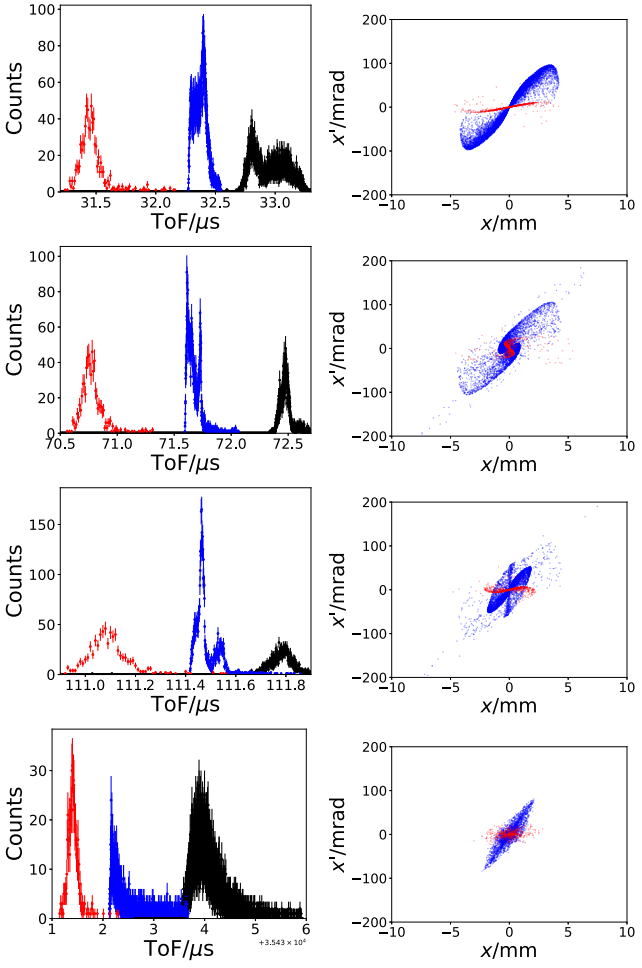


**Fig. 8.** Simulated and measured ToF spectra in transmission (first), after one revolution (second), two revolutions (third) and 900 revolutions (bottom) with a plot of the corresponding transversal emittance for the simulations. The black data points are from measured data, the blue from simulations with the laser ion source and the red from simulations using the cooler buncher ions. The data points of the simulations were taken at a position corresponding to the location of the detector in the measurements. The ion species simulated were singular positively charged ions with a mass of 154 u. For visibility purposes the simulated spectra were moved on the ToF axis.

experimental ionization volume resulting from the overlapping laser beams. The mass of the ions was set to be 154 u. The ions were given a starting kinetic energy of 190 meV, based on a temperature of 1200 °C, with a cone distribution in the direction of the MR-ToF MS with a half angle of 5°. Simulations for a point-like ionization volume never showed the behaviour of multiple peaks in the ToF spectrum. Fig. 8 shows in addition the transversal emittance for increasing number of turns in the MR-ToF. The time structure changes significantly, thus pointing towards the need for better defined emittance of the beam entering the MR-ToF. The experimental results shown in this article were acquired over a span of several months. The performance of the ion-source depends strongly on the laser beam positions and diameters. Changes in these may have led to the situation that a second peak from the same isotope in the ToF spectrum was not present in every experiment.

### 3.3. MR-ToF MS characterization

In addition to the time structure, the behaviour with respect to the relative efficiency $\epsilon$ and mass resolving power $R$ was investigated. For

this purpose, the ions were trapped for different numbers of revolutions and the ToF signal after ejection was evaluated. For the efficiency determination, the number of ions reaching the detector is analysed as a function of the number of revolutions. The efficiency for every dataset is normalized to the respective efficiency in transmission mode. As can be seen in Fig. 9, the measured relative efficiency $\epsilon$ drops in all cases quite steeply in the first few revolutions and begins to settle after about 100 revolutions. The experimental results show the largest drop and settle at about 20%, while the simulations with the laser ion source settle to about 35%. The difference can be attributed to deviations of the ion beam from the central axis. This assumption is supported from the observation of some periodic staggering in the obtained efficiency for more than 200 revolutions indicating spatial oscillations of the ion trajectory within the MR-ToF MS. This staggering effect is known in the collaboration and arises from the path of the ions not being a perfectly closed trajectory inside the MR-ToF MS but it moving slowly over the number of revolutions originating different trajectories of ions while exiting the MR-ToF MS. When comparing the emittances in Fig. 8, the loss of efficiency visible in the top part of Fig. 9 can be generally explained by a too large transversal emittance of the injected ion beam. This was cross checked in another simulation for ions with a Gaussian ToF and energy distribution. This follows the measured distribution (c.f. Section 3.2), while transversal emittance was set to zero. This simulation was done up until 100 revolutions showing no ion loss. As seen in Fig. 8 the ToF spectrum with one revolution features multiple peaks. For an increasing number of revolutions the intensity ratio between the ToF peak with the highest intensity and the other ones shifts in favour of the former. This indicates that from the multiple existing ToF components there is one favoured due to it having the lowest transversal emittance. Since this is the only ToF components persisting, it can be assumed that most, if not all, of the losses can be attributed to these other higher-emittance ToF components.

The emittance figures in Fig. 8 were all taken at the same position, which is the location of the detector in the real setup. The emittance from the simulated laser ion source reveals multiple different patterns within itself over the course of the revolutions. After 900 revolutions there is only one pattern visible. The evolution of the emittance shows a change in shape for both the ions from the laser ion source (blue), as well as the ones from the cooler buncher (red). This shows that there are some changes in ion trajectory and therefore the path and angle at which they get ejected out of the MR-ToF MS over the course of multiple revolutions. For the red emittance, the overall volume remains nearly constant throughout its evolution, whereas the volume of the blue emittance shrinks significantly until the end. After 900 revolutions, which is already beyond the point of ion losses, both emittances look similar in shape, albeit being rotated with respect to one another.

From the ToF spectra, the mass resolving power $R$ was determined as a function of the number of revolutions as shown in the lower part of Fig. 9. It is defined as $R = \frac{m}{\Delta m} = \frac{t}{2\Delta t}$. Due to the appearance of multiple peaks, the standard deviation $\sigma_{\mathrm{ToF}}$ of the obtained ToF was calculated. For the mass resolving power, $\Delta t = 2\sqrt{2 \cdot \ln 2} \cdot \sigma_{\mathrm{ToF}}$ was assumed. The highest experimentally achieved mass resolving power was approximately 25 000, which was limited due to a broadening of the peaks and an asymmetric peak shape, which was also observed in the simulations. The simulations with ions from the cooler buncher resulted in well-defined singular peaks visible in each ToF spectrum, corresponding to a mass resolving power of 100 000 with a maximum at 4000 revolutions For a species with a mass of 154 u, this would lead to a total ToF of 157.5 ms.

Fig. 10 illustrates the possibility of in-trap beam purification via the in-trap deflector electrodes. Here, the laser for the FES was set to 30 373.1280 $\mathrm{cm}^{-1}$ at which the isotopes $^{147}$Sm, $^{148}$Sm and $^{149}$Sm have been ionized simultaneously. A mixed ion sample containing these isotopes was injected into the MR-ToF MS and trapped. The timing for the in-trap lift for the ejection was set so that $^{148}$Sm was ejected

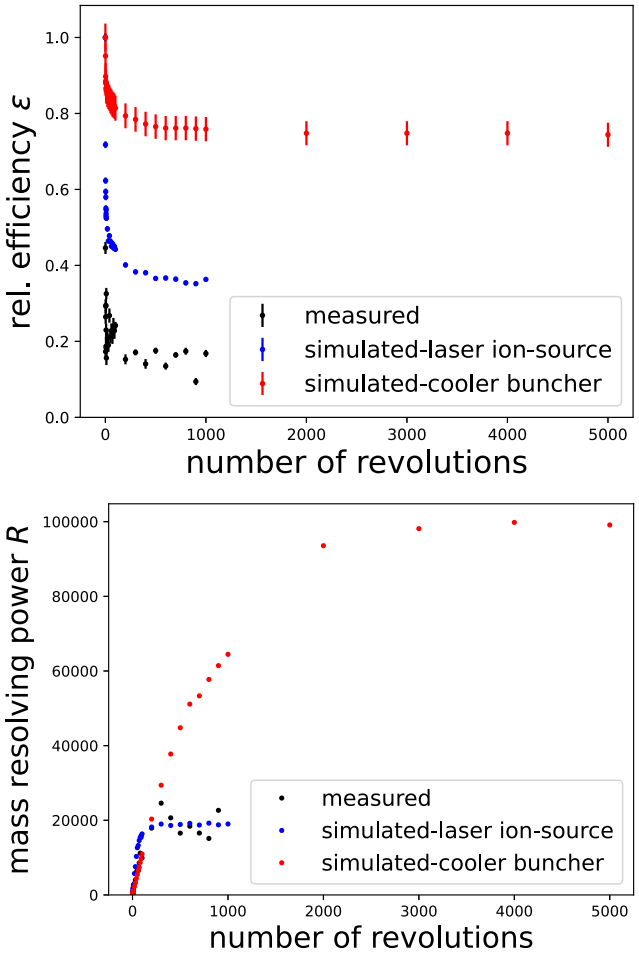


**Fig. 9.** Top: Efficiency $\epsilon$ relative to the number of transmitted ions without trapping of the MR-ToF MS for different number of revolutions. Bottom: Mass resolving power $R$ of the MR-ToF MS against the number of revolutions. The experimental data (black) is compared to the simulated ion source (blue) and the expected behaviour with the cooler buncher (red). The given errorbars are statistical uncertainties from the measured counts or the number of investigated ions, respectively.

after 300 revolutions, which in turn led $^{147}$Sm being ejected after 301 revolutions and $^{149}$Sm after 299 revolutions, as shown in the left panel of Fig. 10 with all isotopes visible in the ToF window. After 57.833 µs in the MR-ToF, which is half of the full trapping time, $^{148}$Sm finished an integer number of revolutions, while the other two isotopes finished half a revolution, leading to a maximum spacial separation between the even mass isotope and the odd mass ones. At this time, the top segment of deflector electrode at the side of the odd mass isotopes was pulsed from 0 V to 100 V for 1 µs. This leads to the result shown in the right panel of Fig. 10 where only the peak of $^{148}$Sm is visible, while the other two peaks are removed.

## 4. Conclusion

Using ToF-assisted resonance ionization laser spectroscopy, multiple laser excitation schemes of samarium were developed and investigated. Here, the mass and field shift constants were determined as well as the hyperfine parameter $\mathcal{A}$ for the excited states in the odd mass numbered isotopes. This provides a basis for on-line laser spectroscopy experiments on neutron-deficient samarium isotopes using the JetRIS technique. Furthermore, first characterizations of an MR-ToF MS for JetRIS were done utilizing a pulsed laser ion source, showing the

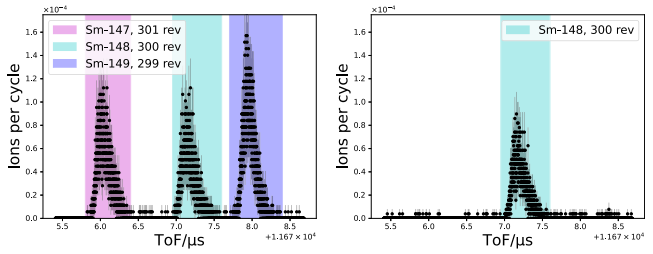


**Fig. 10.** Measured ToF spectra using the deflector electrodes for beam purification. The left figure shows three peaks which were attributed to $^{147}$Sm, $^{148}$Sm and $^{149}$Sm from left to right. The right figure shows the same spectrum while $^{147}$Sm and $^{149}$Sm were deflected during the trapping time. The change in intensity of $^{148}$Sm in both figures is attributed to a change in intensity of the ion source.

potential of combining these two techniques. While this combination still showed caveats in the performance regarding achieved efficiencies and ToF structure, and thus on the mass resolving power, a clear path towards the final integration of the MR-ToF into the JetRIS setup is given with the usage of a cooler buncher for which the design is reported in this work. This upgraded setup will extend the reach of on-line laser spectroscopy experiments to heavy nuclei independent of their decay mode and give access to long-lived nuclides. An interesting nuclide that will become accessible with this setup is $^{254}$Md as well as the aforementioned neutron-deficient samarium isotopes.

## CRediT authorship contribution statement

**Danny Münzberg:** Writing – review & editing, Writing – original draft, Visualization, Project administration, Investigation - Laser spectroscopy & Mass spectrometry, Data analysis - Laser spectroscopy & Mass spectrometry, Conceptualization. **Alexandre Brizard:** Writing – review & editing, Investigation - Cooler buncher, Data analysis - Cooler buncher. **Tim van de Vendel:** Writing – review & editing, Investigation - Cooler buncher, Data analysis - Cooler buncher. **Jana Weyrich:** Writing – review & editing, Investigation - Mass spectrometry, Data analysis - Laser spectroscopy & Mass spectrometry. **Michael Block:** Writing – review & editing, Supervision, Resources, Funding acquisition. **Julia Even:** Writing – review & editing, Resources. **Christian Helmel:** Writing – review & editing, Investigation - early stages mass spectrometry. **Nathalie Lecesne:** Writing – review & editing, Resources. **Sebastian Raeder:** Writing – review & editing, Data analysis. **Daniel Rodríguez:** Writing – review & editing, Investigation - early stages Mass spectrometry. **Hervé Savajols:** Writing – review & editing, Resources. **Klaus Wendt:** Writing – review & editing, Resources, Funding acquisition.

## Declaration of competing interest

The authors declare that they have no known competing financial interests or personal relationships that could have appeared to influence the work reported in this paper.

## Acknowledgements

We gratefully acknowledge the help of the mechanical workshop of the physics institute of the JGU Mainz. This work has been supported by the Bundesministerium für Bildung und Forschung (BMBF, Germany) under project numbers 05P18UMCIA and 05P21UMFN3. T.v.d.V. acknowledges support from the EU Erasmus+ programme, the GET_INvolved Programme of FAIR/GSI GmbH, Darmstadt, Germany and the Marco Polo fund of the University of Groningen, Netherlands and the Bundesministerium für Bildung und Forschung (BMBF, Germany) under grant number 05P21RDFN1. DR acknowledges financial support from the HIM Guest Scientist Program, Germany and from Grant No. PID2022-141496NB-I00 funded by MICIU/AEI/10.13039/501100011033, Germany and by ERDF/EU.

## Data availability

Data will be made available on request.

## References

[1] Witold Nazarewicz, The limits of nuclear mass and charge, Nat. Phys. (ISSN: 1745-2473) 14 (6) (2018) 537–541, http://dx.doi.org/10.1038/s41567-018-0163-3.

[2] S.A. Giuliani, Z. Matheson, W. Nazarewicz, E. Olsen, P.-G. Reinhard, J. Sadhukhan, B. Schuetrumpf, N. Schunck, P. Schwerdtfeger, Colloquium : Superheavy elements: Oganesson and beyond, Rev. Modern Phys. (ISSN: 0034-6861) 91 (1) (2019) 011001, http://dx.doi.org/10.1103/RevModPhys.91.011001.

[3] Odile R. Smits, Christoph E. Düllmann, Paul Indelicato, Witold Nazarewicz, Peter Schwerdtfeger, The quest for superheavy elements and the limit of the periodic table, Nat. Rev. Phys. 6 (2) (2024) 86–98, http://dx.doi.org/10.1038/s42254-023-00668-y.

[4] S. Raeder, M. Block, P. Chhetri, R. Ferrer, S. Kraemer, T. Kron, M. Laatiaoui, S. Nothhelfer, F. Schneider, P. van Duppen, M. Verlinde, E. Verstraelen, Th. Walther, A. Zadvornaya, A gas-jet apparatus for high-resolution laser spectroscopy on the heaviest elements at SHIP, Nucl. Instrum. Methods Phys. Res. Sect. B: Beam Interactions Mater. Atoms (ISSN: 0168583X) 463 (2020) 272–276, http://dx.doi.org/10.1016/j.nimb.2019.05.016.

[5] Jeremy Lantis, Arno Claessens, Danny Münzberg, Julian Auler, Michael Block, Premaditya Chhetri, Christoph E. Düllmann, Rafael Ferrer, Francesca Giacoppo, Manuel J. Gutiérrez, Fedor Ivandikov, Oliver Kaleja, Tom Kieck, EunKang Kim, Mustapha Laatiaoui, Nathalie Lecesne, Vladimir Manea, Steven Nothhelfer, Sebastian Raeder, Jekabs Romans, Elisa Romero-Romero, Antoine de Roubin, Hervé Savajols, Simon Sels, Matou Stemmler, Piet van Duppen, Thomas Walther, Jessica Warbinek, Klaus Wendt, Alexander Yakushev, Alexandra Zadvornaya, In-gas-jet laser spectroscopy of No254 with JetRIS, Phys. Rev. Res. 6 (2) (2024) 023318, http://dx.doi.org/10.1103/PhysRevResearch.6.023318.

[6] Jiguang Li, Vladimir Dzuba, Theoretical study of the spectroscopic properties of mendelevium ( z=101 ), J. Quant. Spectrosc. Radiat. Transfer (ISSN: 00224073) 247 (2020) 106943, http://dx.doi.org/10.1016/j.jqsrt.2020.106943.

[7] Mustapha Laatiaoui, Sebastian Raeder, Laser spectroscopy of the heaviest elements: One atom at a time, Nucl. Phys. News (ISSN: 1061-9127) 29 (1) (2019) 21–25, http://dx.doi.org/10.1080/10619127.2019.1571804.

[8] J. Magill, R. Dreher, Zs. Sóti, Karlsruher nuklidkarte, 11. Auflage, Nucleonica GmbH and Marktdienste Haberbeck GmbH, Karlsruhe and Lage, ISBN: 978-3-00-069180-5, 2022.

[9] M. Schlaich, J. Fischer, P. Fischer, C. Klink, A. Obertelli, A. Schmidt, L. Schweikhard, F. Wienholtz, A multi-reflection time-of-flight mass spectrometer for the offline ion source of the PUMA experiment, Int. J. Mass Spectrom. (ISSN: 13873806) 495 (2024) 117166, http://dx.doi.org/10.1016/j.ijms.2023.117166.

[10] Steven Nothhelfer, Advances in laser spectroscopy of superheavy elements: Resonance ionization spectroscopy on 253,254,255Es and a new gas-jet based high-resolution spectroscopy setup (Ph.D. thesis), Johannes Gutenberg-Universität Mainz, 2022, http://dx.doi.org/10.25358/openscience-6958.

[11] X.F. Yang, S.J. Wang, S.G. Wilkins, R. GarciaF. Ruiz, Laser spectroscopy for the study of exotic nuclei, Prog. Part. Nucl. Phys. (ISSN: 01466410) 129 (2023) 104005, http://dx.doi.org/10.1016/j.ppnp.2022.104005.

[12] R. Pengo, D. Evers, K.E.G. Löbner, U. Quade, K. Rudolph, S.J. Skorka, I. Weidl, Nuclear structure effects in sub-barrier fusion cross sections, Nucl. Phys. A (ISSN: 03759474) 411 (2) (1983) 255–274, http://dx.doi.org/10.1016/0375-9474(83)90392-5.

[13] David A. Dahl, Simion for the personal computer in reflection, Int. J. Mass Spectrom. (ISSN: 13873806) 200 (1–3) (2000) 3–25, http://dx.doi.org/10.1016/S1387-3806(00)00305-5.

[14] Palmer, SIMION 8, 2020, URL https://simion.com.

[15] F. Wienholtz, S. Kreim, M. Rosenbusch, L. Schweikhard, R.N. Wolf, Mass-selective ion ejection from multi-reflection time-of-flight devices via a pulsed in-trap lift, Int. J. Mass Spectrom. (ISSN: 13873806) 421 (2017) 285–293, http://dx.doi.org/10.1016/j.ijms.2017.07.016.

[16] M. Verlinde, R. Ferrer, A. Claessens, C.A. Granados, S. Kraemer, Yu Kudryavtsev, D. Li, P. van den Bergh, P. van Duppen, E. Verstraelen, Single-longitudinal-mode pumped pulsed-dye amplifier for high-resolution laser spectroscopy, Rev. Sci. Instruments 91 (10) (2020) 103002, http://dx.doi.org/10.1063/5.0017985.

[17] W. Gins, R.P. de Groote, M.L. Bissell, C. Granados Buitrago, R. Ferrer, K.M. Lynch, G. Neyens, S. Sels, Analysis of counting data: Development of the SATLAS python package, Comput. Phys. Comm. (ISSN: 00104655) 222 (2018) 286–294, http://dx.doi.org/10.1016/j.cpc.2017.09.012.

[18] G. Audi, O. Bersillon, J. Blachot, A.H. Wapstra, The nubase evaluation of nuclear and decay properties, Nucl. Phys. A (ISSN: 03759474) 729 (1) (2003) 3–128, http://dx.doi.org/10.1016/j.nuclphysa.2003.11.001.

[19] Walter Albertson, The arc spectrum of samarium and gadolinium. Normal electron configurations of the rare earths, Phys. Rev. (ISSN: 0031-899X) 47 (5) (1935) 370–376, http://dx.doi.org/10.1103/PhysRev.47.370.

[20] William Meggers, Charles Corliss, Bourdon Scribner, second ed., Tables of Spectral-Line Intensities Part I - Arranged by Elements, vol. 1, U.S. Department of commerce, National Bureau of Standards, 1975, URL https://digital.library.unt.edu/ark:/67531/metadc13183/m2/1/high_res_d/NBS%20Monograph%20145%20Part1.pdf.

[21] Н. ehкh, В.А. Комаровскй, С[icy][lcy]Ос[tscy][icy][lcy][lcy][yacy]торов с[Pi]ektpa[lcy]ьh[ыx [lcy][icy]h[icy]й [icy] bpemeha [zhcy][icy]зh[icy] вozБy[zhcy][dcy]ehhыx cocтoЯh[icy]й atomob pe[dcy]Koзeme[lcy]ьhыx [ecy][lcy]emehtob c [dcy]octpa[icy]ba[YUcy]щейсЯ 4f-oБo[lcy]oкKoй, J. Quant. Spectrosc. Radiat. Transfer (ISSN: 00224073) 16 (3) (1976) 217–252, http://dx.doi.org/10.1016/0022-4073(76)90066-2.

[22] W.J. Childs, L.S. Goodman, Reanalysis of the hyperfine structure of the 4f66s2F7 multiplet in Sm147,149 , including measurements for the F67 state, Phys. Rev. A (ISSN: 0556-2791) 6 (6) (1972) 2011–2021, http://dx.doi.org/10.1103/PhysRevA.6.2011.

[23] Ninel Nica, Balraj Singh, Nuclear data sheets for A=147, Nucl. Data Sheets (ISSN: 00903752) 181 (2022) 1–474, http://dx.doi.org/10.1016/j.nds.2022.03.001.

[24] Balraj Singh, Jun Chen, Nuclear structure and decay data for A=149 isobars, Nucl. Data Sheets (ISSN: 00903752) 185 (2022) 2–559, http://dx.doi.org/10.1016/j.nds.2022.10.001.

[25] X.U. Zhao-jin, Zhang Xiao-hu, Zhang Wen-na, Huang Chao-hong, Shen Li, Shift of the first ionization threshold of sm atom in electric field, Chin. Opt. (ISSN: 2095-1531) 13 (6) (2020) 1385–1400, http://dx.doi.org/10.37188/CO.2020-0071.

[26] W.C. Martin, Romuald Zalubas, Lucy Hagan, Atomic Energy Levels - the Rare-Earth Elements, National Bureau of Standards, Gaithersburg, MD, 1978, http://dx.doi.org/10.6028/NBS.NSRDS.60.

[27] H. Brand, B. Seibert, A. Steudel, Laser-atomic-beam spectroscopy in sm: Isotope shifts and changes in mean-square nuclear charge radii, Z. Phys. Atoms Nucl. (ISSN: 0340-2193) 296 (4) (1980) 281–286, http://dx.doi.org/10.1007/BF01438521.

[28] Wilfried Nörtershäuser, Christopher Geppert, Nuclear charge radii of light elements and recent developments in collinear laser spectroscopy, in: Christoph Scheidenberger, Marek Pfützner (Eds.), The Euroschool on Exotic Beams, Vol. IV, in: Lecture Notes in Physics, vol. 879, Springer Berlin Heidelberg, Berlin, Heidelberg, ISBN: 978-3-642-45140-9, 2014, pp. 233–292, http://dx.doi.org/10.1007/978-3-642-45141-6{_}6.

[29] G. Münzenberg, W. Faust, S. Hofmann, P. Armbruster, K. Güttner, H. Ewald, The velocity filter ship, a separator of unslowed heavy ion fusion products, Nucl. Instrum. Methods (ISSN: 0029554X) 161 (1) (1979) 65–82, http://dx.doi.org/10.1016/0029-554X(79)90362-8.

[30] Michael Block, Francesca Giacoppo, Fritz-Peter Heßberger, Sebastian Raeder, Recent progress in experiments on the heaviest nuclides at SHIP, La Riv. Del Nuovo Cimento (ISSN: 0393-697X) 45 (4) (2022) 279–323, http://dx.doi.org/10.1007/s40766-022-00030-5.

[31] H. Backe, P. Kunz, W. Lauth, A. Dretzke, R. Horn, T. Kolb, M. Laatiaoui, M. Sewtz, D. Ackermann, M. Block, F. Herfurth, F.P. Heßberger, S. Hofmann, R. Mann, Towards optical spectroscopy of the element nobelium (z= 102) in a buffer gas cell, Eur. Phys. J. D (ISSN: 1434-6060) 45 (1) (2007) 99–106, http://dx.doi.org/10.1140/epjd/e2007-00198-1.

[32] R. Ferrer, M. Verlinde, E. Verstraelen, A. Claessens, M. Huyse, S. Kraemer, Yu. Kudryavtsev, J. Romans, P. van den Bergh, P. van Duppen, A. Zadvornaya, O. Chazot, G. Grossir, V.I. Kalikmanov, M. Nabuurs, D. Reynaerts, Hypersonic nozzle for laser-spectroscopy studies at 17 K characterized by resonance-ionization-spectroscopy-based flow mapping, Phys. Rev. Res. 3 (4) (2021) 043041, http://dx.doi.org/10.1103/PhysRevResearch.3.043041.

[33] Danny Münzberg, Michael Block, Arno Claessens, Rafael Ferrer, Mustapha Laatiaoui, Jeremy Lantis, Steven Nothhelfer, Sebastian Raeder, Piet van Duppen, Resolution characterizations of JetRIS in mainz using 164Dy, Atoms 10 (2) (2022) 57, http://dx.doi.org/10.3390/atoms10020057.

[34] Yu. Kudryavtsev, P. Creemers, R. Ferrer, C. Granados, L.P. Gaffney, M. Huyse, E. Mogilevskiy, S. Raeder, S. Sels, P. van den Bergh, P. van Duppen, A. Zadvornaya, A new in-gas-laser ionization and spectroscopy laboratory for off-line studies at KU leuven, Nucl. Instrum Methods Phys. Res. Sect. B: Beam Interactions Mater. Atoms (ISSN: 0168583X) 376 (2016) 345–352, http://dx.doi.org/10.1016/j.nimb.2016.02.040.

[35] Anjali Ajayakumar, Jekabs Romans, Martial Authier, Yazeed Balasmeh, Alexandre Brizard, Frederic Boumard, Lucia Caceres, Jean-Francois Cam, Arno Claessens, Samuel Damoy, Pierre Delahaye, Philippe Desrues, Wenling Dong, Antoine Drouart, Patricia Duchesne, Rafael Ferrer, Xavier Fléchard, Serge Franchoo, Patrice Gangnant, Sarina Geldhof, Ruben P. de Groote, Fedor Ivandikov, Nathalie Lecesne, Renan Leroy, Julien Lory, Franck Lutton, Vladimir Manea, Yvan Merrer, Iain Moore, Alejandro Ortiz-Cortes, Benoit Osmond, Julien Piot, Olivier Pochon, Sebastian Raeder, Antoine de Roubin, Hervé Savajols, Dominik Studer, Emil Traykov, Juha Uusitalo, Christophe Vandamme, Paul van den Bergh, Piet van Duppen, Klaus Wendt, In-gas-jet laser spectroscopy with S 3 -LEB, Nucl. Instrum. Methods Phys. Res. Sect. B: Beam Interactions Mater. Atoms (ISSN: 0168583X) 539 (2023) 102–107, http://dx.doi.org/10.1016/j.nimb.2023.03.020.

[36] A. O'Hagan, T.O.M. Leonard, Bayes estimation subject to uncertainty about parameter constraints, Biometrika (ISSN: 0006-3444) 63 (1) (1976) 201–203, http://dx.doi.org/10.1093/biomet/63.1.201.